M. Rusconi, G. Borelli, G. Consolati, C. Colombo
Model-Based Analysis of Satellite Telemetry for Thruster Torque Characterization
Journal of Spacecraft and Rockets, Vol. 63, N. 1, p. 349-355, 2026 (published online 06/08/2025)
doi:10.2514/1.a36343

Model-Based Analysis of Satellite Telemetry for Thruster Torque Characterization

Martina Rusconi,* Giacomo Borelli,† Giovanni Consolati,‡ and Camilla Colombo§
Polytechnic of Milan, 20156 Milan, Italy

I. Introduction

THIS work presents a practical and data-driven method for estimating parasitic torque from in-orbit telemetry, offering a valuable tool for diagnosing and validating new propulsion systems directly in their operational environment. The approach is particularly useful in scenarios where detailed prelaunch models are unavailable or incomplete, which is an increasingly common situation as the space industry shifts toward more rapid, cost-effective mission cycles. By enabling the characterization of actuators-induced disturbances directly from flight data, the method supports early performance assessment without the need for extensive ground testing. The actuator considered in the analysis is a thruster located asymmetrically on the satellite and produces an unknown torque that alters the spacecraft attitude when activated. Since no prior model of the thruster is available, the analysis follows a reverse engineering approach: telemetry data, particularly angular velocity measurements, are compared with predictions from a physics-based simulation of the satellite's motion. This baseline model is constructed using data from nonfiring periods and includes a simplified geometry of the satellite, represented as a parallelepiped with fixed solar panels. The workflow begins with filtering and preprocessing the angular velocity data to reduce sensor noise. Next, the satellite's inertial properties are estimated using least-squares fitting techniques, enabling the creation of a reference simulator that captures the nominal dynamics of the system. Once the model accurately reproduces the satellite's motion without actuators activity, it is used to detect deviations occurring during thruster firings. These discrepancies, isolated through anomaly detection methods, are interpreted as evidence of external torque. Assuming the thruster-generated torque remains constant during each firing period, it is estimated by identifying the forcing term that best reconciles the observed and simulated angular velocity profiles. This methodology enables early stage in-orbit characterization of new propulsion technologies, supporting rapid validation without relying on detailed prelaunch models. As space access becomes increasingly affordable, such data-driven approaches reduce the dependency on exhaustive ground testing and accelerate the development cycle. The process integrates elements from health monitoring, model tuning, and in-orbit validation, providing a flexible framework for assessing technologies directly in their operational environment.

II. The Simulator

An orbit and attitude simulation tool has been developed at Politecnico di Milano [1]. The core block of the simulator is modeling and numerical integration of orbital and attitude dynamics under the effect of environmental forces and actions of the actuators. The orbital motion-satellite position $\boldsymbol{r}$, velocity, and acceleration-is described through the perturbed two-body problem in Eq. (1) under the environmental effect $\boldsymbol{a}_{\text{Pert}}$ of gravity acceleration from oblate Earth with spherical harmonics expansion up to 18th-order, atmospheric drag, solar radiation pressure and third body effect from Sun and Moon [2].

$$\ddot{\boldsymbol{r}} + \frac{\mu}{r^3}\boldsymbol{r} = \boldsymbol{a}_{\text{Pert}} \tag{1}$$

The attitude dynamics, with ω identifying angular velocity, is described with the Euler's Eq. (2) where the satellite's rigid body, with inertia $\boldsymbol{J}$, moves under the effect of actuators $\boldsymbol{T}_{\text{Act}}$ (i. e. the thruster effect when on) and environmental perturbations $\boldsymbol{T}_{\text{Env}}$: gravity gradient, atmospheric drag, solar radiation pressure, and magnetic torque [3].

$$\boldsymbol{J}\dot{\boldsymbol{\omega}} + \boldsymbol{\omega} \times \boldsymbol{J}\boldsymbol{\omega} = \boldsymbol{T}_{\text{Env}} + \boldsymbol{T}_{\text{Act}} \tag{2}$$

The simulator models the satellite motion and is used to reproduce the telemetry of the state of the satellite recorded during in-flight tests. The simulation tool accepts satellite model parameters and states as inputs. The telemetry file downloaded from the spacecraft includes data on both orbital and attitude states recorded at discrete times. The orbital position and velocity vectors of the satellite are derived from GPS data, while attitude information, specifically angular velocity and orientation quaternions, is obtained from the Attitude Determination and Control System (ADCS) system, based on filtered data from sun and magnetic field sensors. The telemetry is filtered to reduce noise from sensors acquisition and exploited for model refinement through satellite parameter estimation and for estimation of the parasitic torque acting on the satellite when the thruster is on. In principle, $\boldsymbol{T}_{\text{Act}}$ represents a generic parasitic torque that remains unbalanced in the model. In the following application, we reasonably assume that it primarily captures the effect of the actuators when active, whose influence is expected to dominate over other residual torques.

A. Data Processing

The aim of the work is to characterize the parasitic torque effect acting on the satellite when the engine is on and used as a mean for attitude motion. Therefore, the analysis focuses on angular velocity motion reproduction and data matching. Angular velocity telemetry is affected by noise from sensors and data recording that hinders the knowledge of the initial state of the satellite and may mislead the detection of phenomena that made the dynamics diverge from its predicted path. To address this, the simulator includes an Extended Kalman Filter (EKF) [4] to filter out noise on the angular velocity evolution used as observables, assuming zero-mean Gaussian noise. The EKF is chosen because it effectively handles the nonlinear dynamics typical of satellite motion and is widely recognized for

*Ph.D. Candidate, Department of Aerospace Science and Technology, Via La Masa 34; martina.rusconi@polimi.it (Corresponding Author).

†Post-Doctoral Researcher, Department of Aerospace Science and Technology; giacomo.borelli@polimi.it.

‡Associate Professor, Department of Aerospace Science and Technology; giovanni.consolati@polimi.it.

§Professor, Department of Aerospace Science and Technology; camilla.colombo@polimi.it.

providing accurate and reliable state estimation in such contexts. The filter operates recursively through prediction and correction steps. In the prediction phase, the state and covariance are propagated using the nonlinear dynamics in Eq. (2), following the approach in [5]. In the correction phase, the Kalman gain is computed from the predicted covariance, and the state is updated using the measurement. Since angular velocity is directly measured, the observation Jacobian is the identity matrix. To ensure the covariance matrix remains positive-definite, Cholesky factorization is applied as suggested in [4]. The square root of the covariance is updated during correction following the formulations in [6,7]. To further refine the estimates, Rauch-Tung-Striebel smoothing is applied, filtering backward in time using EKF outputs and an approximate linear state transition matrix from [8]. Full derivations are provided in [4].

Filter initialization requires measurement error covariances, typically based on sensor noise, and process noise covariances, affected by model uncertainties. Often, the covariances definition follows from trial and error campaigns. To avoid this lengthy procedure, this work explores three systematic estimation methods for noise and process covariances, $\boldsymbol{R}$ and $\boldsymbol{Q}$ respectively: Indirect Correlation Method (ICM) [9] which analyzes the autocorrelation matrix of the innovation sequence from a suboptimal steady-state Kalman filter to obtain consistent estimates of the covariances, Maximum-Likelihood Method (MLM) [10] which optimizes $\boldsymbol{Q}$ and $\boldsymbol{R}$ to minimize the negative log-likelihood function of the innovations samples of a suboptimal EKF, and Covariance Matching Method (CMM) [11] which estimates the state and the covariances at the same time so that the theoretical and empirical innovations match statistically.

The initial state covariance is also systematically defined, following the approach in [12], where the uncertainty in the initial state is estimated using known bounds of possible values that the initial state can assume. The method assumes the error between the guessed and true initial state is half the width of this interval and uses it to construct a diagonal covariance matrix.

A sensitivity analysis using synthetic tests compared ICM, MLM, and CMM under purely environmental dynamics. Initial position $\boldsymbol{r}$, velocity $\boldsymbol{v}$, angular velocity $\boldsymbol{\omega}$, quaternions $\boldsymbol{q}$, and inertia $\boldsymbol{J}$ are given in Table 1. Motion was simulated 100 times over 30 minutes with Gaussian noise, with standard deviations in Table 1, and with random modeling errors on inertia within 10–20%. Initial process and noise covariance ($\boldsymbol{Q}$ and $\boldsymbol{R}$) were defined as in Table 1. Tests were sampled every 5 and 10 s. The results are shown in terms of Root Mean Squared Error (RMSE) of Eq. (3) between true and EKF filtered samples of $\boldsymbol{\omega}$.

$$\mathrm{RMSE} = \sqrt{\frac{1}{N}\sum_{k=1}^{N} \|\boldsymbol{\omega}_{\mathrm{EKF}} - \boldsymbol{\omega}_{\mathrm{true}}\|^2} \tag{3}$$

Figure 1a shows RMSE for all tests, with bold lines separating different sampling rates. Figure 1b reports average RMSE of samples grouped by same method and sampling time. As seen in Fig. 1, RMSE slightly increases with lower sampling. Being more conservative to data, MLM yields the lowest average RMSE, though CMM shows less variability than MLM and ICM, which has the widest spread.

In Fig. 2, one case of the sensitivity analysis is provided. Figure 2a shows the evolution of the diagonal terms of the covariance matrix throughout EKF filtering. The filter improves the ω estimates at the beginning, keeping performance for the rest of the data. In Fig. 2b, the noisy angular velocity samples are compared against the filtered ones (continuous lines) and smoothed ones (dotted lines).

B. Parameters Estimation

Simulations are affected by modeling errors, particularly inertia, which is a key uncertainty in attitude dynamics. The preliminary evaluation of mass properties prior to launch is typically affected by uncertainty up to 10–20%, and its influence on the dynamics is clear from Fig. 3, that shows 100 simulations of the same free motion with random inertia errors uniformly sampled within the range of 10% to 20% of the nominal values.

Table 1 Initial state and inertia parameters, standard deviations of the Gaussian noise and covariances

$[\boldsymbol{r} \quad \boldsymbol{v} \quad \boldsymbol{\omega} \quad \boldsymbol{EA}]$	$\boldsymbol{J}$
$\begin{bmatrix} -2633.610\ \mathrm{km} & 5.57\ \mathrm{km/s} & 0.1°/\mathrm{s} & 9.5° \\ 2833.860\ \mathrm{km} & -31.20\ \mathrm{km/s} & 0.3°/\mathrm{s} & 5° \\ 5715.882\ \mathrm{km} & 41.21\ \mathrm{km/s} & 0.05°/\mathrm{s} & 5° \end{bmatrix}$	$\begin{bmatrix} 32.1 & -0.252 & -2.07 \\ -0.252 & 35.5 & -1.19 \\ -2.07 & -1.19 & 25.8 \end{bmatrix}\ \mathrm{kgm}^2$
$[\sigma_r \quad \sigma_v \quad \sigma_\omega \quad \sigma_{EA}]$	$\boldsymbol{Q}_0$ / $\boldsymbol{R}_0$
$[3\ \mathrm{km} \quad 0.05\ \mathrm{m/s} \quad 0.1°/\mathrm{s} \quad 10°]$	$\begin{bmatrix} 1e-5 & 0 & 0 \\ 0 & 1e-5 & 0 \\ 0 & 0 & 1e-5 \end{bmatrix}$ / $\begin{bmatrix} \sigma_\omega^2 & 0 & 0 \\ 0 & \sigma_\omega^2 & 0 \\ 0 & 0 & \sigma_\omega^2 \end{bmatrix}$

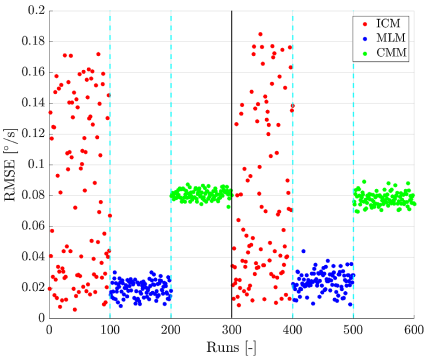

a) RMSE of the tests. Black lines divide tests sampled at 5 s (left) and at 10 s (right). Blue dashed lines divide covariance estimation methods

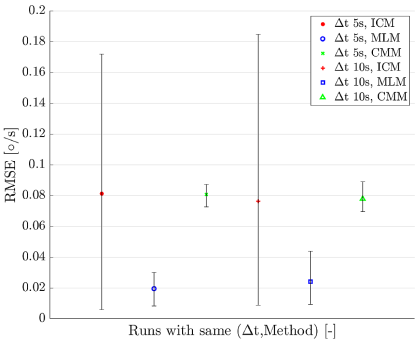

b) Average RMSE on the samples sharing same sampling time and covariance estimation method. Variation bars are also shown

Fig. 1 Overall RMSE results and averages.

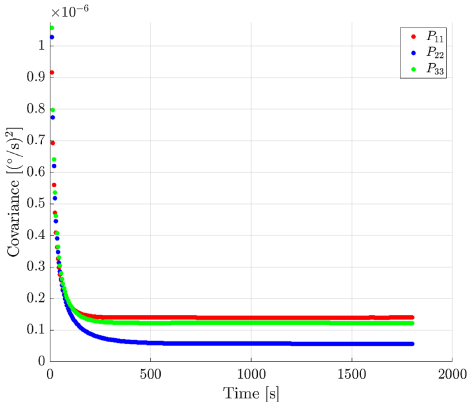

a) Evolution of the diagonal terms of the angular velocity covariance matrix

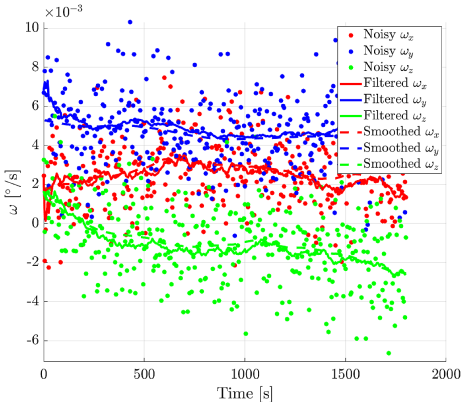

b) Noisy data (single dots) comparison with filtered data (continuous lines) and additionally smoothed data (dotted lines) of the angular velocity components

Fig. 2 EKF filtering action of one sample of the sensitivity analysis.

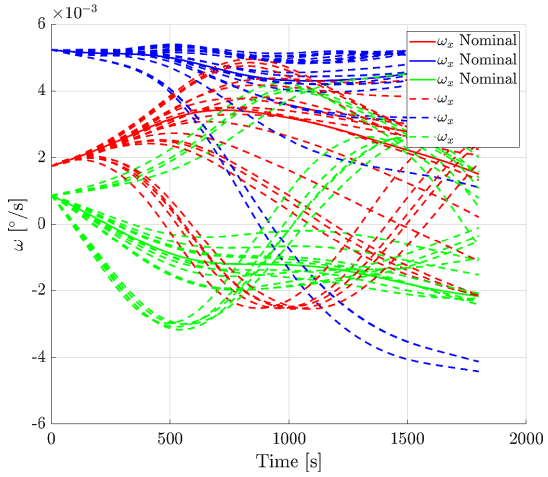

Fig. 3 Angular velocity components evolution in time of a reference scenario with inertia of each sample randomly chosen within ±[10–20%] of the nominal ones.

To improve anomaly detection, this work incorporates parameter uncertainty into the EKF $\boldsymbol{Q}$ matrix, following [12]. In addition to the advantages that this approach can provide, preliminary parameters estimation has been added to improve the simulation. In literature, several methods are found to retrieve mass properties from telemetry data on the satellite state. The typical approach exploits Linear Least Squares (LLS) optimization on data batches exiting the EKF, and, for the application of the work, it is based on the formulation of Eq. (2) as a linear system in the inertia values [13,14]. Additionally, in order to have an estimation technique capable of working on real-time data and considering also for varying parameters, a Recursive Least Squares (RLS) approach has been investigated, integrating it into the Kalman filter [14,15].

The most suited approach for the analysis at hand has been defined by comparing LLS and RLS methods via Monte Carlo analysis with inputs from Table 1. Initial inertia covariances followed [12], with up to 20% error on the true values. Both methods were tested on 30-min synthetic data of the satellite state with the noise model of Sec. II.A, sampled every 5 s. To ensure persistence of excitation, known torques from Table 2 were applied. The Kalman filter used both constant and time-varying $\boldsymbol{Q}$ from [12].

RMSE, defined in Eq. (3), was used to evaluate improvements in angular velocity reproduction after inertia estimation. Table 3 reports the percentage of cases where RMSE improved. Inertia accuracy was assessed by the percentage error of estimates relative to true values as in Eq. (4), with Table 4 reporting the share of estimates within 5% and 10% of the true values.

Table 2 Torque profiles investigated, each counting 60 samples

	Values
Magnitude of one component	$\pm[1e-4, 5e-4, 1e-3, 5e-3]$ Nm
Profile	Constant excitation along x body axis
	Constant excitation along y body axis
	Constant excitation along z body axis
	Sequential constant excitation along x, y and z body axis
	Constant excitation along the three body axes at once

Table 3 Percentage of samples with improved RMSE after inertia estimation, comparing LLS and RLS[a]

Method				
LLS			RLS	
38%			77%	
RLS method				
$\boldsymbol{Q}_{\text{fix}}$			$\boldsymbol{Q}(t)$	
78%			76%	
Single-x	Single-y	Single-z	Sequential	Three-axis
71%	62%	80%	79%	94%

[a]Results grouped by $\boldsymbol{Q}$ method and torque excitation are shown for tests processed with RLS.

$$J_{\text{error}_i} = \left| \frac{J_{\text{estimated}_i} - J_{\text{true}_i}}{J_{\text{true}_i}} \right| * 100 \tag{4}$$

Focus is on moments of inertia, which dominate dynamics and are less error-prone. RLS outperformed LLS, so results by $\boldsymbol{Q}$ type and excitation condition are shown only for RLS. Constant and time-varying $\boldsymbol{Q}$ gave similar results. Excitation type is crucial; single-axis excitation gives varying results depending on inertia values, combining sequential single-axis excitation, and applying torque on all axes simultaneously yields the best inertia estimation for most samples.

Figure 4 shows the time evolution of inertia estimates for one sensitivity analysis sample, including covariance matrix diagonal terms (Fig. 4a) and parameter values (Fig. 4b), using the RLS method. The method significantly improves initial estimates, with values progressively converging to the nominal ones.

C. Constant Torque Estimation

After inertia estimation, an augmented Kalman filter is used to jointly estimate angular velocity and torque components,

Table 4 Percentage of samples with inertia estimation errors below 5% and 10%

Category	Error ≤ 5%						Error ≤ 10%					
	J_{xx}	J_{xy}	J_{xz}	J_{yy}	J_{yz}	J_{zz}	J_{xx}	J_{xy}	J_{xz}	J_{yy}	J_{yz}	J_{zz}
LLS	**32%**	3%	18%	**29%**	11%	**34%**	**43%**	7%	29%	**45%**	28%	**48%**
RLS	**44%**	9%	17%	**49%**	27%	**48%**	**71%**	17%	35%	**67%**	43%	**71%**
RLS method												
$\boldsymbol{Q}_{\text{fix}}$	**45%**	9%	19%	**52%**	28%	**47%**	**69%**	19%	36%	**69%**	46%	**72%**
$\boldsymbol{Q}(t)$	**43%**	8%	15%	**46%**	25%	**50%**	**72%**	15%	35%	**65%**	41%	**70%**
Single x axis excitation	**53%**	8%	20%	**54%**	23%	**38%**	**78%**	10%	33%	**73%**	37%	**55%**
Single y axis excitation	**23%**	8%	8%	**23%**	14%	**32%**	**43%**	17%	27%	**29%**	33%	**51%**
Single z axis excitation	**40%**	0%	14%	**56%**	23%	**51%**	**68%**	11%	23%	**73%**	39%	**87%**
Sequential excitation of single axis	**43%**	11%	23%	**45%**	33%	**48%**	**83%**	20%	48%	**80%**	50%	**73%**
Three axis excitation	**61%**	16%	22%	**66%**	40%	**73%**	**83%**	28%	47%	**81%**	57%	**88%**

LLS and RLS methods are compared, with results for RLS grouped by $\boldsymbol{Q}$ method and torque excitation.

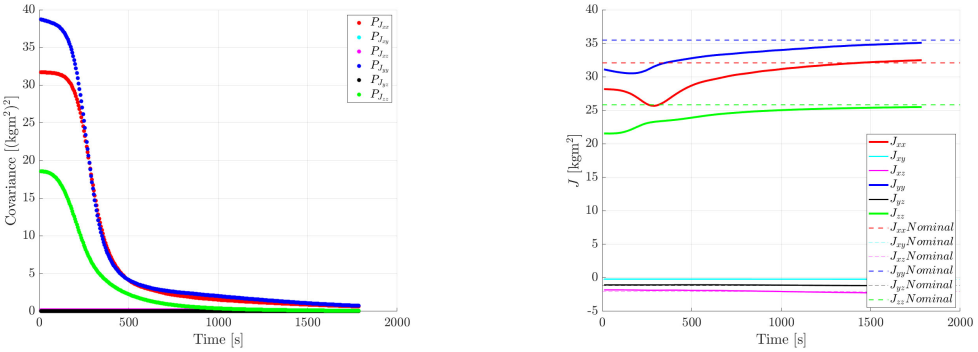

a) Evolution of the diagonal terms of the inertia covariance matrix

b) Inertia estimates over time, with continuous lines converging toward nominal values (dotted lines)

Fig. 4 Inertia estimation through RLS method of one sample of the sensitivity analysis.

following [4,16]. A joint vector is built by concatenating the state derivative from Eq. (2) and the parameters vector rate of change to obtain the augmented dynamics in Eq. (5). The process and measurement Jacobians and the covariance matrices are augmented accordingly, as in Eqs. (6) and (7). Then, the EKF algorithm is applied to sequentially estimate the current state and update the model with the current best estimate of the parameters.

$$\dot{x} = \begin{bmatrix} \dot{\boldsymbol{\omega}} \\ \dot{\boldsymbol{T}} \end{bmatrix} = \begin{bmatrix} \boldsymbol{J}^{-1}(-\boldsymbol{\omega} \times \boldsymbol{J}\boldsymbol{\omega} + \boldsymbol{T}) \\ \boldsymbol{0}_{3\times1} \end{bmatrix} \tag{5}$$

$$\boldsymbol{J}_f = \begin{bmatrix} \frac{\delta\dot{\boldsymbol{\omega}}}{\delta\boldsymbol{\omega}} & \frac{\delta\dot{\boldsymbol{\omega}}}{\delta\boldsymbol{T}} \\ \frac{\delta\dot{\boldsymbol{T}}}{\delta\boldsymbol{\omega}} & \frac{\delta\dot{\boldsymbol{T}}}{\delta\boldsymbol{T}} \end{bmatrix} = \begin{bmatrix} \frac{\delta\dot{\boldsymbol{\omega}}}{\delta\boldsymbol{\omega}} & \boldsymbol{J}^{-1} \\ \boldsymbol{0}_{3\times3} & \boldsymbol{0}_{3\times3} \end{bmatrix} \quad \boldsymbol{J}_h = \begin{bmatrix} \boldsymbol{I}_{3\times3} & \boldsymbol{0}_{3\times3} \end{bmatrix} \tag{6}$$

$$\boldsymbol{P}_0 = \begin{bmatrix} \boldsymbol{P}_{0_{\omega_{3\times3}}} & \boldsymbol{0}_{3\times3} \\ \boldsymbol{0}_{3\times3} & \boldsymbol{P}_{0_{T_{3\times3}}} \end{bmatrix} \quad \boldsymbol{Q} = \begin{bmatrix} \boldsymbol{Q}_{\omega_{3\times3}} & \boldsymbol{0}_{3\times3} \\ \boldsymbol{0}_{3\times3} & \boldsymbol{Q}_{T_{3\times3}} \end{bmatrix}$$
$$\boldsymbol{R} = \begin{bmatrix} \boldsymbol{R}_{\omega_{3\times3}} & \boldsymbol{0}_{3\times3} \\ \boldsymbol{0}_{3\times3} & \boldsymbol{R}_{T_{3\times3}} \end{bmatrix} \tag{7}$$

The performance of the joint filter was tested through a sensitivity analysis on samples with varying applied torques, using initial conditions from Table 1. Its performance builds on the EKF filtering and inertia estimation previously applied (Secs. II.B and II.A). Residual inertia modeling errors from the results in Sec. II.B after RLS were evaluated in terms of average residual torque and applied torques to estimate were set above this threshold. Torque components were randomly selected within $\pm[1e-3, 1e-4]$ Nm. Two test durations (10 and 30 min) were analyzed, with 100 samples each. Torque estimates were initialized at 0 with covariance set to 1.

Table 5 Percentage of samples whose estimation error on the torque components is below 5% and 10%

Category	Error ≤ 5%			Error ≤ 10%		
	T_x	T_y	T_z	T_x	T_y	T_z
10 min	34%	31%	43%	54%	56%	71%
30 min	9%	20%	41%	21%	33%	65%
All	40%	37%	57%	72%	66%	85%

Only constant torques were tested. Table 5 shows the percentage of samples with final estimation errors below 5% and 10% for each component, defined as in Eq. (8).

$$T_{\text{error}_i} = \left| \frac{T_{\text{estimated}_i} - T_{\text{true}_i}}{T_{\text{true}_i}} \right| * 100 \tag{8}$$

Shorter test durations (10 min) yielded better results, as longer tests accumulate more residual errors. To reflect this, final results in the final row of Table 5 include only the first 100 data points from both 10- and 30-min tests. The method from [4,16] estimates torque within 10% error in most cases.

Figure 5 shows torque estimation over time for one sensitivity test: component values (Fig. 5b) and diagonal terms of the torque covariance matrix (Fig. 5a). The torque estimates are improved at the beginning of the filtering action and then oscillate in time around the nominal values.

III. Applications

The methods of the previous sections are applied in sequence for validation on synthetic and real data. Synthetic tests use the

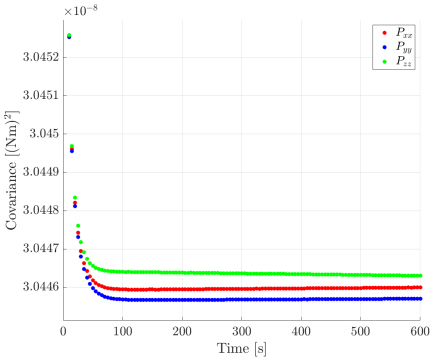

a) Evolution of the diagonal terms of the torque covariance matrix

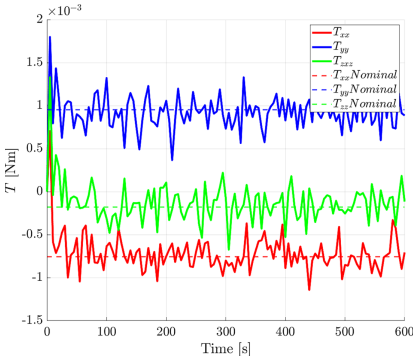

b) Torque component estimates over time (continuous lines), converging toward nominal values (dotted lines)

Fig. 5 Torque estimation through extended Kalman filter of one test of the sensitivity analysis in Sec. II.C.

Table 6 Percentage of samples with improved angular velocity RMSE after inertia estimation

Simulation	Improved RMSE
After $\boldsymbol{J}$ estimation	83%

Table 7 Percentage of samples whose estimation error on inertia is below 5% and 10%

Error ≤ 5%						Error ≤ 10%					
J_{xx}	J_{xy}	J_{xz}	J_{yy}	J_{yz}	J_{zz}	J_{xx}	J_{xy}	J_{xz}	J_{yy}	J_{yz}	J_{zz}
54%	39%	44%	**54%**	38%	**68%**	**88%**	74%	76%	**96%**	72%	**97%**

Table 8 Percentage of samples whose estimation error on the torque components is below 5%, 10%, and 20%

Error ≤ 5%			Error ≤ 10%			Error ≤ 20%		
T_x	T_y	T_z	T_x	T_y	T_z	T_x	T_y	T_z
13%	19%	28%	33%	33%	50%	60%	51%	79%

simulator to generate the telemetry on the satellite state, while the real case uses telemetry from D-Orbit.[¶]

A. Application to Synthetic Data

One hundred tests were run by propagating the satellite motion for 10 min, using initial conditions from Table 1. Ten to twenty percent random inertia errors were added. The goal was to estimate applied torques, defined as in Sec. II.C, with each component within $[1e-4, 1e-2]$ Nm. For each test, three parallel 30-minute data sets were also generated for inertia estimation, with torque inputs as in Sec. II.B. Following the workflow: data were filtered with an EKF, inertias refined via RLS using the extra datasets, and torque estimated from the improved model. RMSE was used to assess accuracy in angular velocity reproduction; the percentage of samples with improved RMSE appears in Table 6. Final inertia and torque estimation accuracy (below 5%, 10%, and 20% error) is reported in Tables 7 and 8.

Despite the challenge of torque estimation from noisy data, combining filtering, parameter estimation, and the recursive method in Sec. II.C yields torque estimates within 20% error for most samples. Figure 6 shows angular velocity evolution for one test: initial noisy data, nominal dynamics, and the final simulation after inertia and torque estimation. The close match of the final simulation

[¶]Data available online at https://www.dorbit.space/.

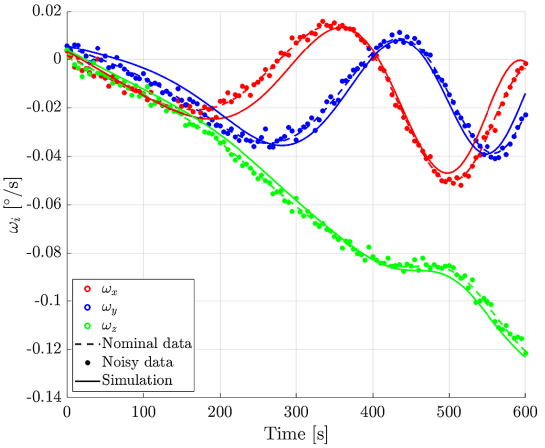

Fig. 6 Angular velocity evolution for one test in Sec. III.A: nominal data (dotted), noisy data (dots), and final simulation (solid lines).

with the nominal data confirms the effectiveness of the joint Kalman filter in capturing the parasitic torque.

B. Application to Real Data

A similar analysis was performed using real telemetry from a known maneuver, where constant torque was applied via reaction wheels. Orbital and attitude data were recorded onboard every 5 s. Inertia estimates with 20% uncertainty were provided by the company. The simulator used the inputs from Table 1. As shown in Figs. 7a and 7b, the EKF effectively filtered the data, which showed low noise. This test was exploited for parameters estimation, given that the actuator torque provided by the reaction wheels was available from manipulation of the recorded data [3]. Figures 7c and 7d show that angular velocity simulation aligns more closely with recorded data after inertia updates. Table 9 reports percentage changes in estimated inertias relative to initial guesses. RMSE values in Table 10 quantify performance across stages: raw against simulation data, filtered against simulated, and after inertia refinement. The lowest RMSE occurs after updating the model, supporting the visual results.

After parameters refinement, the joint EKF approach was tested on a shorter test, applying a torque of $[0.0011, -0.0011, -0.0011]$ Nm. Figure 7e shows the estimated torque components, which converge to the reference values with correct signs and near-nominal magnitude, though modeling errors and time-accumulating discrepancies still affect the results.

IV. Conclusions

As access to space becomes more affordable, in-orbit testing offers a practical alternative to extensive ground campaigns for early

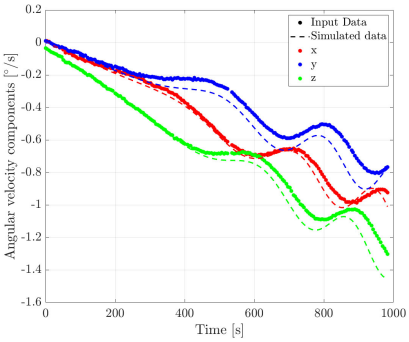

a) Angular velocity time evolution: noisy data (dots), simulation from the unprocessed data (dashed lines)

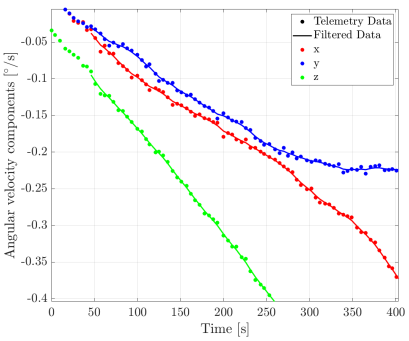

b) Zoomed view of the angular velocity time evolution:noisy (dots) and filtered data (continuous lines)

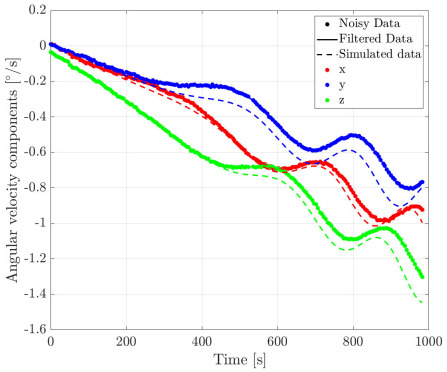

c) Angular velocity time evolution: noisy data (dots), filtered (continuous lines) and simulation after filtering (dashed lines)

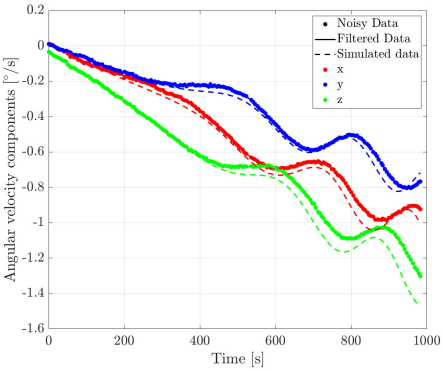

d) Angular velocity time evolution: noisy data (dots), filtered (continuous lines) and simulation after inertia estimation (dashed line)

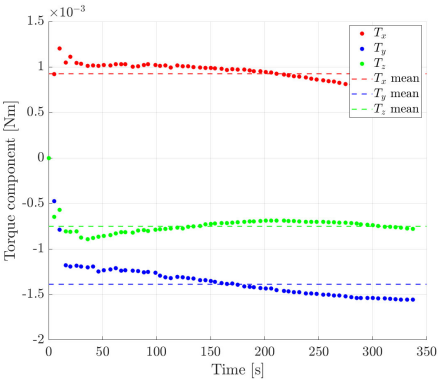

e) Joint EKF estimation of the torque at each step of the test

Fig. 7 Data before and after filtering (Figs. 7a and 7b), before and after inertia estimation (Figs. 7c and 7d) and final torque estimates (7e).

Table 9 Estimated inertia values and their percentage change from initial guesses

Inertia parameters	J_{xx}	J_{xy}	J_{xz}	J_{yy}	J_{yz}	J_{zz}
Estimated value	**31.5**	−0.252	−2.07	**39.3**	−1.18	**25.5**
$\Delta J_{\%}$	**−1.98%**	−0.104%	+0.203%	**+10.6%**	−0.773%	**−1.34%**

Table 10 RMSE between noisy angular velocity and simulation (Fig. 7a), filtered data and simulation (Fig. 7c), and filtered data and simulation after inertia estimation (Fig. 7d)

Simulation	**RMSE, °/s**
No data processing	0.1040
After EKF	0.1024
After inertia estimation	0.0864

stage validation of new technologies. This work proposes a method to estimate the constant torque generated by a thruster mounted on a satellite and used as a mean for attitude motion, using only angular velocity telemetry and without prior knowledge of the performance of the thruster. The approach combines data-driven techniques with physics-based simulation, integrating Kalman filtering, inertia estimation via recursive least squares, and a joint extended Kalman filter to identify the residual torque during thruster firings. Sensitivity analyses have been performed on the Kalman filter initialization techniques and on parameter and torque estimation approaches confirming the methods' robustness, with inertia estimation errors below 10% and torque estimation within ±20% accuracy. The workflow was tested on real satellite telemetry of its attitude state, demonstrating improved simulation accuracy after inertia refinement. Despite inherent model limitations

and external uncertainties, the method proves effective in characterizing unknown propulsion systems in orbit.

Acknowledgments

The authors acknowledge Mr. Marco Cazzaniga and the team from D-Orbit for the in-flight data, and Mr. Vincenzo Tirella and Mr. Luca Iaboni from GenerGo for providing the study case scenario.

References

[1] Rusconi, M., Borelli, G., Tirella, V., and Colombo, C., "Modelling and Simulation of an on-Orbit Experiment for Testing a Novel Engine Technology," *Proceedings of 73rd International Astronautical Conference*, Paper IAC-22,C1,IP,19,x73745, International Astronautical Federation, 2022, https://hdl.handle.net/11311/1223394.

[2] Vallado, D., *Fundamentals of Astrodynamics and Applications*, Microcosm Press, Hawthorne, CA, 2013, pp. 538–590.

[3] Markley, L., and Crassidis, J., *Fundamentals of Spacecraft Attitude Determination and Control*, Springer, New York, 2014, pp. 403–424, Chap. Environment models.
https://doi.org/10.1007/978-1-4939-0802-8

[4] Haykin, S., *Kalman Filters*, Wiley, New York, 2001, pp. 1–21, Chap. 1.
https://doi.org/10.1002/0471221546.ch1

[5] Kim, D., Yang, S., and Lee, S., "Rigid Body Inertia Estimation Using Extended Kalman and Savitzky-Golay Filters," *Mathematical Problems in Engineering*, Vol. 2016, June 2016, pp. 1–7.
https://doi.org/10.1155/2016/2962671

[6] Andrews, A., "A Square Root Formulation of the Kalman Covariance Equations," *AIAA Journal*, Vol. 6, No. 6, 1968, pp. 1165–1166.
https://doi.org/10.2514/3.4696

[7] Kaminski, P. G., Bryson, A. E., and Schmidt, S. F., "Discrete Square Root Filtering: A Survey of Current Techniques," *IEEE Transactions on Automatic Control*, Vol. 16, No. 6, 1971, pp. 727–736.
https://doi.org/10.1109/TAC.1971.1099816

[8] Bellar, A., and Si Mohammed, M. A., "Satellite Inertia Parameters Estimation Based on Extended Kalman Filter," *Journal of Aerospace Technology and Management*, Vol. 11, Dec. 2019, p. 3.
https://doi.org/10.5028/jatm.v11.1016

[9] Noriega, G., and Pasupathy, S., "Adaptive Estimation of Noise Covariance Matrices in Real-Time Preprocessing of Geophysical Data," *IEEE Transactions in Geoscience and Remote Sensing*, Vol. 35, No. 5, 1997, pp. 1146–1159.
https://doi.org/10.1109/36.628782

[10] Bavdekar, V. A., Deshpande, A. P., and Patwardhan, S. C., "Identification of Process and Measurement Noise Covariance for State and Parameter Estimation Using Extended Kalman Filter," *Journal of Process Control*, Vol. 21, No. 4, 2011, pp. 585–601.
https://doi.org/10.1016/j.jprocont.2011.01.001

[11] Duník, J., Straka, O., Kost, O., and Havlík, J., "Noise Covariance Matrices in State-Space Models: A Survey and Comparison of Estimation Methods-Part I," *International Journal of Adaptive Control and Signal Processing*, Vol. 31, No. 11, 2017, pp. 1505–1543.
https://doi.org/10.1002/acs.2783

[12] Schneider, R., and Georgakis, C., "How to NOT Make the Extended Kalman Filter Fail," *Industrial and Engineering Chemistry Research*, Vol. 52, No. 9, 2013, pp. 3354–3362.
https://doi.org/10.1021/ie300415d

[13] Kim, D. H., Yang, S., Cheon, D. I., Lee, S., and Oh, H. S., "Combined Estimation Method for Inertia Properties of STSAT-3," *Journal of Mechanical Science and Technology*, Vol. 24, No. 8, 2010, pp. 1737–1741.
https://doi.org/10.1007/s12206-010-0521-2

[14] Yang, S., Lee, S., Lee, J. H., and Oh, H. S., "New Real-Time Estimation Method for Inertia Properties of STSAT-3 Using Gyro Data," *Transactions of the Japan Society for Aeronautical and Space Sciences*, Vol. 58, No. 4, 2015, pp. 247–249.
https://doi.org/10.2322/tjsass.58.247

[15] Peck, M. A., "Attitude Determination for Gyrostats in Non-Equilibrium Spins from Infrequent Vector Observations," *AIAA Guidance, Navigation, and Control Conference and Exhibit*, AIAA Paper 2000-3946, 2000.
https://doi.org/10.2514/6.2000-3946

[16] Schwartz, J., and Hall, C., "Comparison of System Identification Techniques for a Spherical Air-Bearing Spacecraft Simulator," *Astrodynamics Specialist Conference*, AAS Paper 03-611, 2003, https://www.researchgate.net/publication/228757000.

P. Ghosh
Associate Editor